



Impact of lanthanum ions on magnetic and dielectric properties of cobalt nanoferrites

I. Kartharinal Punithavathy¹ · A. Rajeshwari¹ · S. Johnson Jeyakumar¹ · N. Lenin² · B. Vigneshwaran³ · M. Jothibas¹ · B. Arunkumar¹

Received: 28 March 2020 / Accepted: 28 April 2020 / Published online: 11 May 2020
© Springer Science+Business Media, LLC, part of Springer Nature 2020

Abstract

Lanthanum-doped cobalt nanoferrites $\text{CoLa}_x\text{Fe}_{2-x}\text{O}_4$ ($X = 0.00$ to 0.08) were synthesized by using sol–gel method. A cubic spinel structure was confirmed by using X-ray diffraction pattern. A band obtained at 583 cm^{-1} recorded by Fourier transform infrared spectrum confirmed the presence of metal oxide spinel nanoferrites. The bandgap energy has increased with addition of La^{3+} ions by using ultraviolet diffuse reflectance spectrum. The grain boundary contribution is greater than that of grain contribution due to small crystal size, which was confirmed by an impedance analysis. The dielectric constant and dielectric losses decreased with increasing frequencies. The binding energy of La, Co, Fe and O were determined by X-ray photoelectron spectroscopy. The magnetic studies were analyzed through vibrating sample magnetometer. The hysteresis loop revealed the soft ferromagnetic nature.

1 Introduction

Recently, spinel nanoferrites have been used in numerous technological and scientific applications [1], i.e., low loss magnetic core materials, hyperthermia, memory devices, drug delivery, antenna rods, gas sensors, microwave-absorbing materials, super capacitors, solar cell, and high-frequency devices [2–4]. Basic formula of spinel nanoferrites is AB_2O_4 , where A and B represent a divalent and trivalent metal cations [5]. The spinel ferrites are classified into three types such as normal spinel structure, inverse spinel structure, and intermediate spinel structure. In normal spinel ferrites, divalent ions are at tetrahedral A-site and trivalent ions are in octahedral B-site; in inverse spinel structure, half of the trivalent ions are at B-site and half at A-site and the remaining ions are distributed in octahedral B-site, whereas intermediate spinel structure possesses the intermediate

stage between the normal and inverse spinel ferrites [6]. From the different spinel ferrite materials, CoFe_2O_4 is the best challenging ferromagnetic material due to its better properties, such as high Curie temperature, high coercivity, reasonable saturation magnetization, high mechanical and chemical stability [7, 8]. Recent years, rare earth elements substituted spinel nanoferrites have special attention in developing their physical properties such as grain size and cation distribution at tetrahedral and octahedral sites [9, 10]. The spinel nanoferrites are the best advisable materials used for absorption of electromagnetic radiation (EMR) in different ways such as ceramic tiles, sheets, and powders [11]. Electromagnetic interference (EMI) has got most promising applications in communication systems such as radar systems, computers, and mobile phones [12, 13]. The EMI affects electronically controlled systems and also damages human health. It causes device interrupt, generate distorted images, increase clutter on radar due to system to system interruption during EMI [14]. To circumvent these EMI troubles, EMR is preferred, which has the ability of absorbing unwanted electromagnetic signals. Rare earth-doped nanoferrites have unique and important applications in electronic devices, transformer cores, magnetic recordings, radar signals, high-frequency circuits, and telecommunication. The doping of lanthanum (La^{3+}) ions which are having unpaired electrons in the 4f orbital tends normally to non-magnetic state. However, replacing smaller ionic radii Fe^{3+}

✉ I. Kartharinal Punithavathy
profpunithaphysics@gmail.com

¹ Department of Physics T.B.M.L College, Porayar, Nagapattinam 609307, India

² Centre for Nano Science and Technology, K.S. Rangasamy College of Technology, Tiruchengode 637215, India

³ Centre for Nanoscience and Nanotechnology, International Research Centre, Sathyabama Institute of Science and Technology, Chennai 600119, India

ions into La^{3+} ions at the octahedral site (B) to the ferrites leads to enhance the magnetic and electrical properties of the spinel nanoferrites used for microwave frequency applications [15–17]. The magnetic saturation (m_s) decreases with an increase in the concentration of rare earth content in Li, Co, and Ni spinel nanoferrites [18]. Azadmanjiri et al. [12] describes, that the stability for transformer core where EMI is gently reduced and can avoid predicting false image in telecommunication system. Lanthanum-doped cobalt ferrites are synthesized by various techniques such as the sonication technique [17], mechanical milling technique [8], coprecipitate method [21], sonochemical method [1], hydrothermal method [19], and sol–gel technique [20]. The spinel nanoferrites were synthesized by sol–gel technique which overcomes the difficulties in co-precipitate technique [21].

In this study, lanthanum-doped cobalt nanoferrites $\text{CoLa}_x\text{Fe}_{2-x}\text{O}_4$ ($X=0.00$ to 0.08) were prepared by using sol–gel method. The obtained lanthanum-doped cobalt nanoferrites were characterized by X-ray diffraction (XRD) for phase and structural identification, ultraviolet diffuse reflectance spectroscopy (UV-DRS) to identify the optical properties, and Fourier transform infrared spectroscopy (FTIR) for checking the metal oxides presence. The field emission scanning electron microscopy (FESEM) and energy-dispersive X-ray analysis (EDX) were used to understand the surface morphology and elemental analysis. Magnetic and electrical properties were evolved using vibrating sample magnetometer (VSM) and Impedance spectroscopy. The obtained results were analyzed and utilized for the application of electronic devices in microwave frequency.

2 Materials and experimental procedure

2.1 Materials

High pure grade Merck precursors such as cobalt nitrate ($\text{Co}(\text{NO}_3)_2 \cdot 6\text{H}_2\text{O}$), lanthanum nitrate ($\text{La}(\text{NO}_3)_3 \cdot 6\text{H}_2\text{O}$), ferric nitrate ($\text{Fe}(\text{NO}_3)_3 \cdot 9\text{H}_2\text{O}$), ammonia (NH_4OH), citric acid ($\text{C}_6\text{H}_8\text{O}_7 \cdot \text{H}_2\text{O}$), and deionized water were used.

2.2 Experimental procedure

The $\text{CoLa}_x\text{Fe}_{2-x}\text{O}_4$ ($X=0.00, 0.02, 0.04, 0.06, 0.08$) nanoferrites were prepared by sol–gel technique in the following approach. The measured precursors were dissolved with 100 ml of deionized water to obtain a uniform mixture of the precursor materials. The final mixture was continuously stirred at a temperature of 80°C for 1 h. Further, ammonia was added drop wise to the ferrite solution to attain the pH value of 7. Finally the dark solution was obtained and dried in hot air oven at fixed temperature of 60°C for 24 h. The dried nanoparticles were collected and sintered

in muffle furnace at 500°C for 2 h. At next, sintered nanopowders were grinded for 15 min to obtain byproduct-free nanoparticles. Thus, obtained nanopowders were calcined at 1000°C for 24 h. The schematic diagram for preparation of $\text{CoLa}_x\text{Fe}_{2-x}\text{O}_4$ nanoferrites is shown in Fig. 1.

2.3 Characterization of the $\text{CoLa}_x\text{Fe}_{2-x}\text{O}_4$ nanoferrites

The crystallite size and structural properties of the prepared $\text{CoLa}_x\text{Fe}_{2-x}\text{O}_4$ ($X=0.00$ to 0.08) nanoferrites were made by XRD (SHIMADZU-XRD 6000) technique with $\text{CuK}\alpha$ radiation source, at the 2θ range from 20° to 80° , operated at 40 kV and 30 mA. The chemical interaction and functional groups obtained in the prepared $\text{CoLa}_x\text{Fe}_{2-x}\text{O}_4$ nanoferrites were determined by FTIR spectra (SHIMADZU-UV 18,000) ranging from 4000 to 400 cm^{-1} at RT (room temperature). The surface morphology and elemental composition were analyzed using FESEM with an EDAX (Quanta FEG 250). The optical properties of the synthesized samples were analyzed using an UV-DRS spectrum and the absorption wavelength was noted from 200 to 400 nm. The electrical property of the synthesized $\text{CoLa}_x\text{Fe}_{2-x}\text{O}_4$ nanoferrites was revealed using Impedance spectroscopy with the frequency range of Hz to 7 MHz at room temperature (30°C) (Biologic SP-300), Silver coating was applied to the pellet for good Ohmic contact. X-ray photoelectron spectroscopic (XPS) studies were made using an

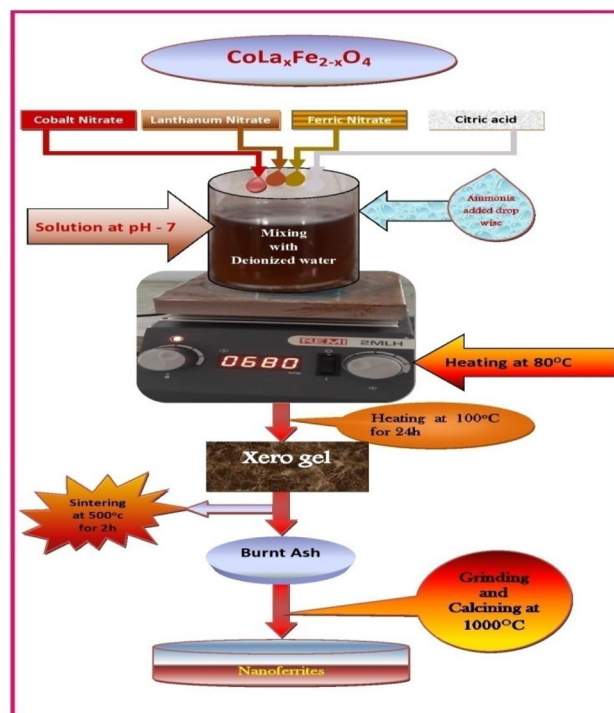


Fig. 1 Schematic diagram for preparation of $\text{CoLa}_x\text{Fe}_{2-x}\text{O}_4$ nanoferrites

(ALU-PHI5000) AUG spectrometer with monochromatic Al K α (26.00 eV) radiation. Magnetic studies were assessed using VSM (Lakeshore VSM 7140) at room temperature (RT) with an applied magnetic field of -15 to $+15$ KOe.

3 Results and discussion

3.1 Structural analysis

XRD patterns of $\text{CoLa}_x\text{Fe}_{2-x}\text{O}_4$ for all the samples with series of $X=0.00$ to 0.08 , calcined at 1000°C are shown in Fig. 2. The obtained peaks are related to cubic spinel ferrites crystal structure and are matched with the standard JCPDS file no 22-1086. The peaks at 30.08° , 35.43° , 43.05° , 53.44° , and 56.97° correspond to the crystal planes (220), (311), (400), (422), and (511), respectively [22, 23]. The average crystal size of the synthesized nanoferrites was estimated using Debye's Scherrer equation [24].

$$D = \frac{k\lambda}{\beta \cos\theta} \quad (1)$$

where k is a Scherrer constant (0.9), λ is the wavelength of X-ray beam, β is the full width half maximum (FWHM),

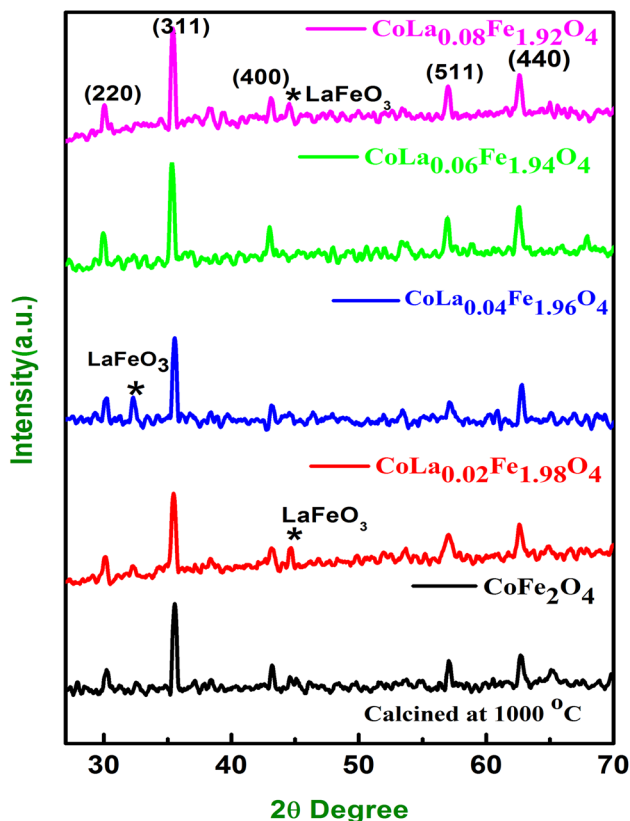


Fig. 2 X-ray diffraction pattern of prepared $\text{CoLa}_x\text{Fe}_{2-x}\text{O}_4$ ($X=0.00$ to 0.08) nanoferrites calcined at 1000°C

and θ is the Bragg's diffraction angle. The crystallite size of the ferrites decreases from 42 to 18 nm with increasing dopants concentration from $X=0.00$ to 0.08 . The La^{3+} ion having ionic radius of 1.06 \AA has larger ionic radii compared with Fe^{3+} ionic radius 0.67 \AA . Therefore, it is difficult to displace Fe^{3+} ion in CoFe_2O_4 spinel cubic nanoferrites. So, few La^{3+} ions could present at grain boundaries. This larger ionic radius of La^{3+} ions form pressure on the grains and therefore crystal size decreases with increasing La content [25]. The emergence of small amount of orthoferrite phase LaFeO_3 also appears with La^{3+} content of ($X=0.02, 0.04, 0.08$). The ionic radius of La^{3+} ion is 1.06 \AA , which is higher than that of the Fe^{3+} ion (0.67 \AA), and hence, the amount of Fe^{3+} ions replaced by La^{3+} ions is limited and hence there is a solubility limit for the replacement of Fe^{3+} ions by La^{3+} ions. Thus, it is expected that an excess substitution of La^{3+} ions tends to aggregate around the grain boundaries in the form of LaFeO_3 .

The lattice constant for the prepared nanoferrites is calculated using Nelson-relay function [26]:

$$a = d_{\text{hkl}} \sqrt{h^2 + k^2 + l^2} \quad (2)$$

where d is inter planar distance, a is the lattice constant, and hkl are Miller indices. The value of lattice constant is 8.37 \AA which is in agreement with the reported value [27]. Lattice constant increases monotonically with increasing La^{3+} ions which is due to the substitution of both Co^{2+} ions with ionic radius of 0.78 \AA and Fe^{3+} ions with ionic radius of 0.64 \AA by the larger La^{3+} ions with ionic radius of 1.06 \AA in Co–Fe–La spinel lattice [28]. The volume of unit cell increases from 587.3 to 600.9 \AA^3 with the increase in La^{3+} concentration which occurs due to a increase in the lattice constant. X-ray density of the CoFe_2O_4 nanoparticles was calculated using the following equation [28]:

$$d_x = \frac{Zm}{Na^3} \quad (3)$$

where N_a is Avogadro's number, m is the molecular weight of the sample, a^3 is the volume of the unit cell, and Z is the basic unit cell for the cubic spinel structure which contains 8 ions. X-ray density decreases from 5.685 to 5.403 g/cm^3 with an increase in La^{3+} ion concentration in cobalt ferrite nanoparticles, which may possibly due to the increase in unit cell volume. The volume of the unit cell is inversely proportional to the X-ray density. The bulk density (d_B) was calculated using the mentioned equation [26]:

$$d_m = \frac{m}{\pi r^2 t} \quad (4)$$

where r is the radius of the pellet, m is the mass of the pellet, and t is the thickness of the pellet. The bulk density of lanthanum-doped cobalt nanoferrites was noticed to decrease

from 2.6085 to 2.0173 g/cm³ with the increase of lanthanum ions. As compared to X-ray density, bulk density was less due to the presence of pores which mainly depend on calcined conditions [29]. The surface area (S) was estimated using the following expression [30]:

$$S = 6/d_X D \quad (5)$$

where d_X is the X-ray density and D is the crystallite size of the nanoparticles. The surface areas (S) are increased with an increase in La³⁺ ions which attribute to a decrease in crystal size. The porosity (P) was calculated using the following relation [30]:

$$P = (1 - d_B/d_X) \% \quad (6)$$

The percentage of porosity increases from 5.0 to 6.4% which may be due to a decrease in bulk density with an increase in La³⁺ concentrations. Structural parameters such as X-ray density, crystal size, dislocation density, micro-strain, lattice constant, volume of unit cell, surface area, bulk density, and porosity were determined and are listed in Table 1.

3.2 Optical properties

The influence of lanthanum on cobalt nanoferrites was studied by using UV-DRS spectra is shown in Fig. 3. The UV-DRS spectrum has overcome UV-visible absorption spectroscopy in its capability to evaluate the optical properties of powdered nanoparticles. UV-visible absorption has larger scattering effect when compared to UV-DRS spectra [17]. The absorbance values are 226.6, 224.7, 223.3, 222.5, and 222.0 nm as shown in Fig. 3. The E_g of the prepared nanoferrites was obtained energy-dependant relation as follows [17]:

$$E_g = \frac{hc}{\lambda} \quad (7)$$

where c is the velocity of light, h is the Planck's constant, and λ is the wavelength of the absorption.

The indirect and direct bandgap energy values of lanthanum-doped cobalt nanoferrites were calculated using the following relation [17]:

$$h\nu\alpha = (h\nu - E_{gap})^n \quad (8)$$

where ν is the frequency, h is the plank's constant, α is the absorbance coefficient, and n is the different types of electronic transition ($n = 1/2$ and 2) for bandgap (indirect and direct) transition, respectively.

In Fig. 3a, direct bandgap energy demonstrates the Taue plot between $(\alpha E_{\text{photon}})^2$ vs E_{phot} and the E values were 1.45, 1.50, 1.53, 1.55, and 1.56 eV. In Fig. 3b, indirect bandgap energy demonstrates the Taue plot between $(\alpha)^{1/2}$ vs E_{phot} and the bandgap energy values of prepared nanoferrites were 1.73, 1.86, 1.93, 1.97, and 2.06 eV, respectively.

The absorbance and bandgap energy values of the lanthanum-doped cobalt nanoferrites are listed in Table 2. The bandgap energy shifts from red region to blue region for doped La³⁺ ions. These shifts are attributed to 3d-4s spin interchange between Fe ions and La ions. However, the lanthanum-doped cobalt nanoferrite bandgap energies vary based on the Brus equation [31].

3.3 Functional group analysis

The FTIR spectra of prepared nanoferrites are depicted in Fig. 4. The transmittance spectra were obtained from the vibrational peaks appropriate to citric acid used in sol-gel technique which was acquired by stretching vibrations appropriate are to metal-oxygen band of around 583 cm⁻¹ to form spinel structure (Table 3).

The broad and strong stretching peak obtained which indicates the O-H stretching due to the available water vapor in the prepared sample at 3437 cm⁻¹ [32]. The bending vibration of CH₂ carbon chain was observed with peak 2921 cm⁻¹. The peaks are at 1745 cm⁻¹ corresponding to the C-H bending absorption of carboxyl group. Then 1149 cm⁻¹ is the C=O stretching vibration due to nitrogen group [33]. In these cubic structure ferrites Fe³⁺ ions placed tetrahedral A-sites as well as octahedral B-sites.

Table 1 Structural parameters of prepared CoLa_XFe_{2-*X*}O₄ ($X=0.00$ to 0.08) nanoferrites optimized calcination temperature at 1000 °C

Composition	Crystal size (D) (nm)	Dislocation density (δ) / $m^2 E+15$	Micro strain (ϵ) $X10^{-3}$	Lattice constant (a) Å	Volume of unit cell (a^3) Å ³	X-ray density (ρ_{XRD}) (g/cm ³)	Surface area (S_{XRD}) (m ² /g)	Bulk density (d_B) (g/cm ³)	Porosity (%)
$X=0.00$	42	0.55	0.849	8.37	587.30	5.68	25.12	2.68	5.0
$X=0.02$	37	0.72	0.977	8.37	587.30	5.64	28.72	2.61	5.2
$X=0.04$	34	0.85	1.058	8.40	593.95	5.54	31.83	2.57	5.3
$X=0.06$	25	1.56	1.429	8.42	596.96	5.47	43.81	2.45	5.6
$X=0.08$	18	2.85	1.933	8.43	600.99	5.40	61.68	2.01	6.4

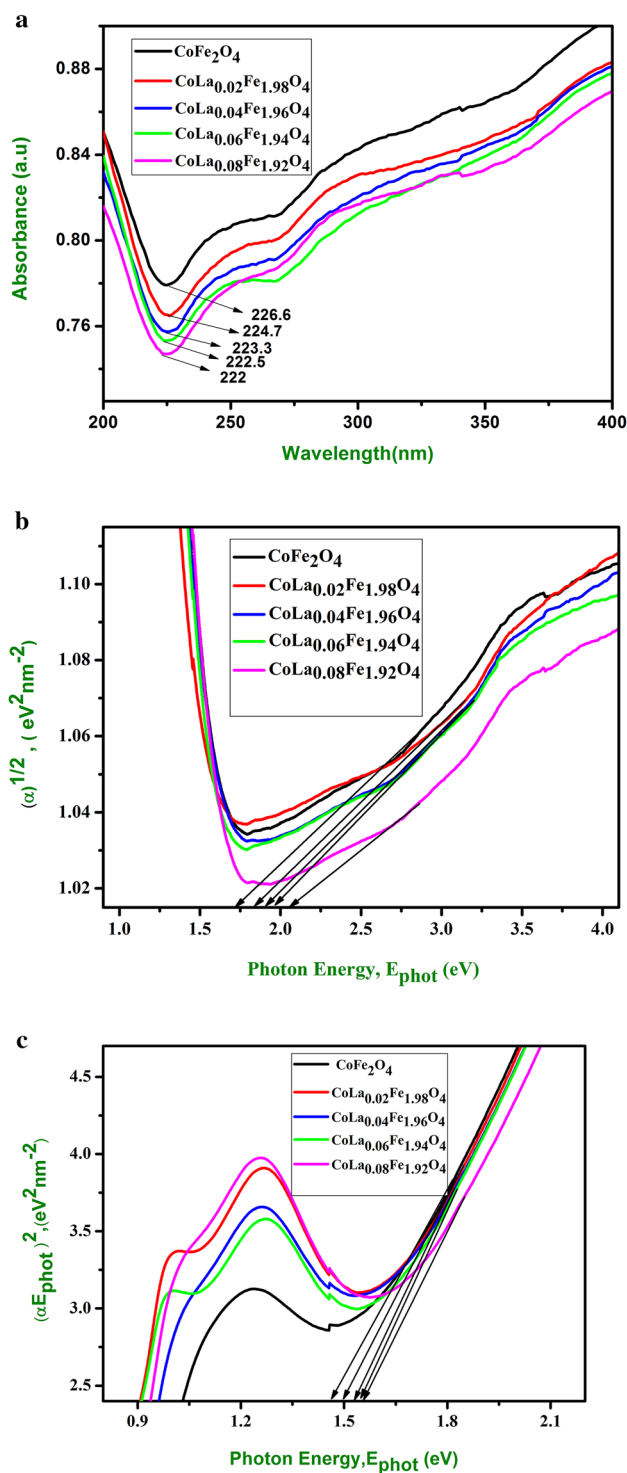


Fig. 3 Absorbance spectra of prepared nanoferrites $\text{CoLa}_X\text{Fe}_{2-X}\text{O}_4$ ($X=0.00$ to 0.08) from UV-DRS spectra. **a** Indirect bandgap energy of prepared nanoferrites $\text{CoLa}_X\text{Fe}_{2-X}\text{O}_4$ ($X=0.00$ to 0.08) from UV-DRS spectra. **b** Direct bandgap energy of prepared nanoferrites $\text{CoLa}_X\text{Fe}_{2-X}\text{O}_4$ ($X=0.00$ to 0.08) from UV-DRS spectra

Table 2 Optical parameters of prepared $\text{CoLa}_X\text{Fe}_{2-X}\text{O}_4$ ($X=0.00$ to 0.08) nanoferrites

Composition	Absorbance (nm)	Indirect band-gap energy (eV)	Direct band-gap energy (eV)
$X=0.00$	226.6	1.73	1.45
$X=0.02$	224.7	1.86	1.50
$X=0.04$	223.3	1.93	1.53
$X=0.06$	222.5	1.97	1.55
$X=0.08$	222.0	2.06	1.56

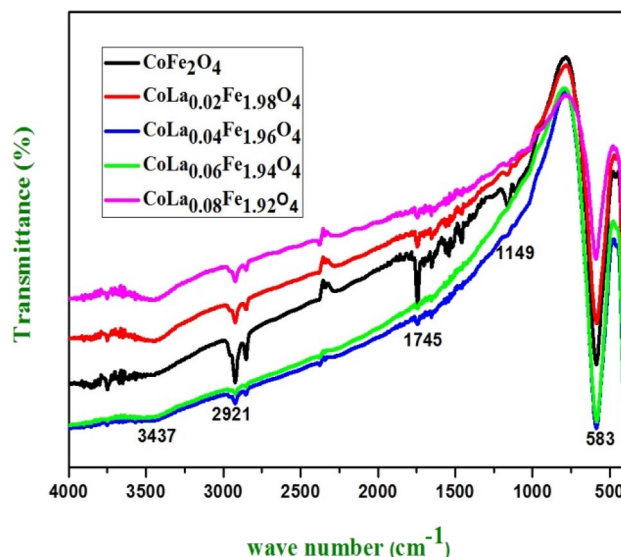


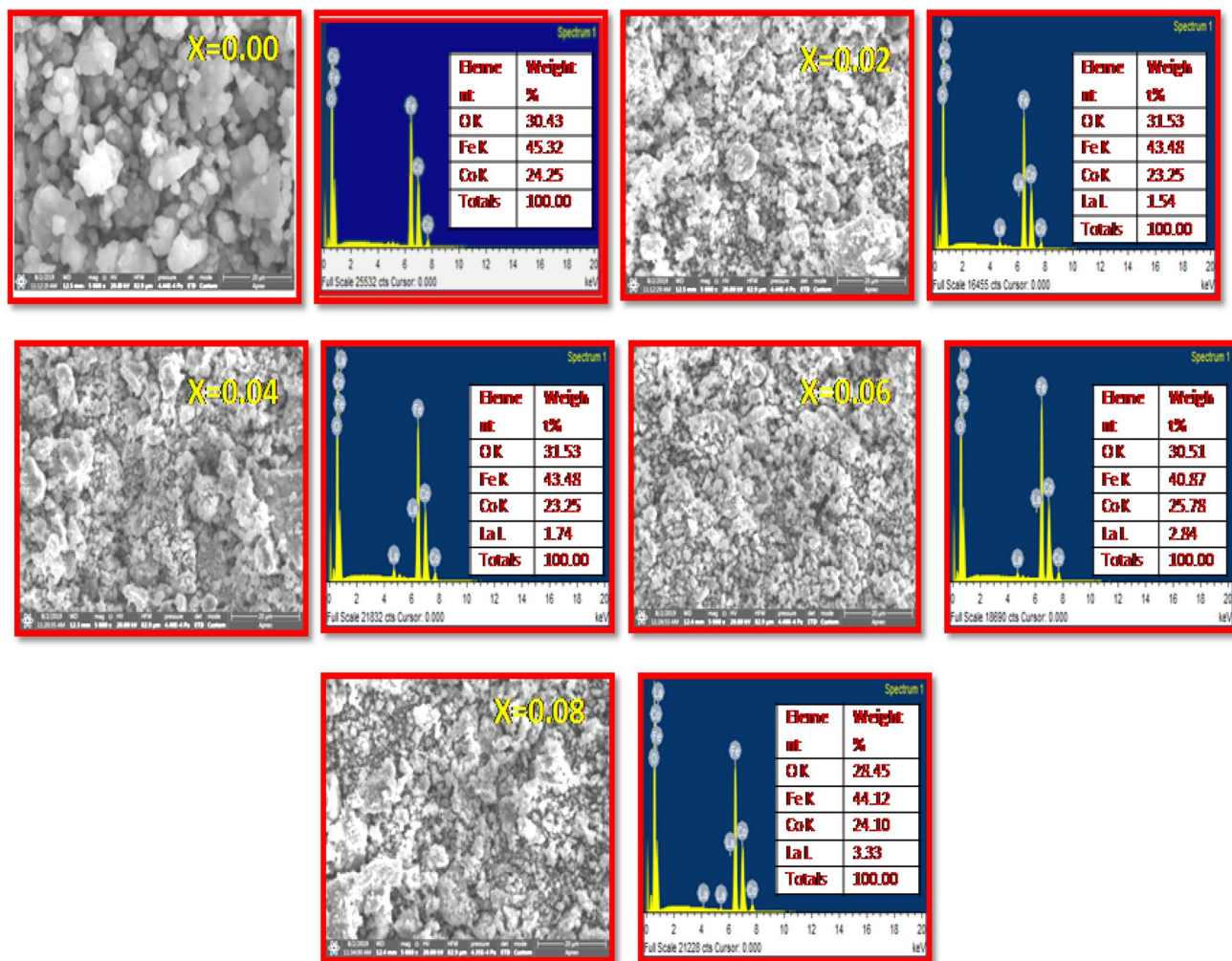
Fig. 4 FTIR spectra of prepared $\text{CoLa}_X\text{Fe}_{2-X}\text{O}_4$ ($X=0.00$ to 0.08) nanoferrites

3.4 Surface morphology with EDAX

The FESEM images of lanthanum-doped cobalt nanoferrites were used to study surface morphology. Figure 5 denotes that the prepared nanoferrites were spherical in shape with some agglomeration. This agglomeration of grain structure was mainly due to small crystallite size, calcinating process and magnetic nature of all the crystallites form together and promotes cluster and also gets agglomerated [34, 35]. Magnetic force or weak Vander Waals bonds plays a major role in holding these agglomerations in contact [36]. In the obtained result, grain size was decreased with an increase in La^{3+} ions. EDAX spectra of lanthanum-doped cobalt nanoferrites correspond to the elements Fe, O, Co, and La, which is presented in Fig. 5 ($X=0.02$ to 0.08) where absent of La peaks is observed for ($X=0.00$).

Table 3 Functional parameters of prepared $\text{CoLa}_x\text{Fe}_{2-x}\text{O}_4$ ($X=0.00$ to 0.08) nanoferrites

S. no	Vibrational assignments	Experimental absorption (cm^{-1})				
		$X=0.00$	$X=0.02$	$X=0.04$	$X=0.06$	$X=0.08$
1	Metal–oxygen stretching vibration	583	583	583	583	583
2	C=O stretching vibration	1149	1149	1149	1149	1149
3	C–H bending vibration of carboxyl group	1745	1745	1745	1745	1745
4	CH_2 bending vibration of carbon chain	2921	2921	2921	2921	2921
5	O–H stretching vibration	3437	3437	3437	3437	3437

**Fig. 5** FESEM with EDAX images of the prepared $\text{CoLa}_x\text{Fe}_{2-x}\text{O}_4$ ($X=0.00$ to 0.08) nanoferrites

3.5 XPS studies

The X-ray photoelectron spectroscopy (XPS) analysis was used to investigate oxidation state and elemental composition of prepared nanoferrites. Figure 6 brings a wide scan spectrum of pure and lanthanum-doped cobalt nanoferrites in the range of 0–980 eV. In the long-range spectrum as in Fig. 6e, it can be clearly shown that the elemental and oxidation states of Co 2p, Fe 2p, La 3d, O 1s, and C 1s are present.

No other elements were found, which proves the purity of prepared nanoferrites. The narrow scan spectrum of O 1s shown in Fig. 6a clearly indicates a peak at 529.06, 535.76, and 535.96 eV for pure and lanthanum-doped cobalt nanoferrites. These obtained peaks were due to the presence of O^{2-} in the nanoferrites [37, 38]. The narrow scan spectrum of O 1s shown in Fig. 6b, clearly indicate a peak at 529.06, 535.76 and 535.96 eV for pure and lanthanum doped cobalt nanoferrites. These obtained peaks were due to the presence

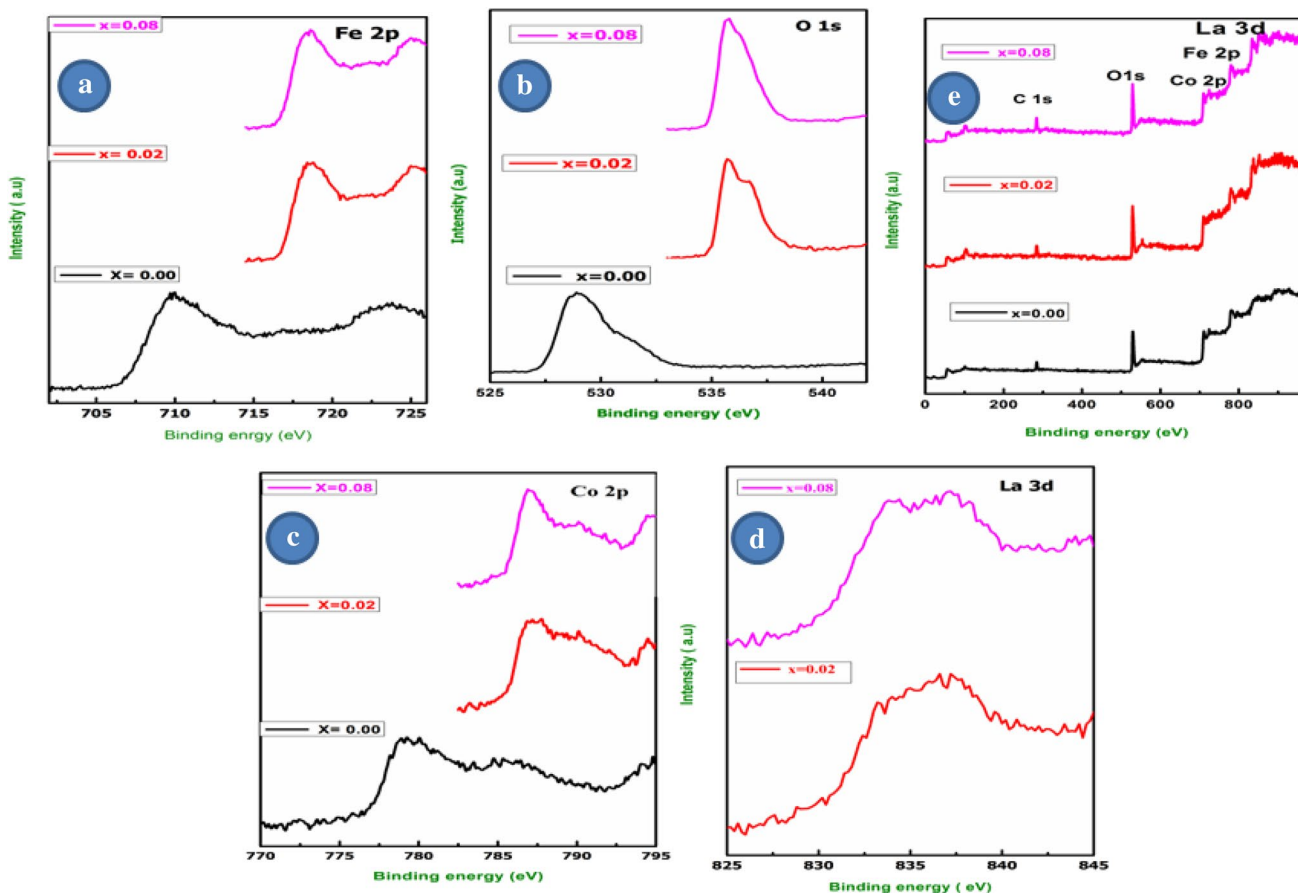


Fig. 6 XPS spectra of the prepared $\text{CoLa}_x\text{Fe}_{2-x}\text{O}_4$ ($X=0.00$ to 0.08) nanoferrites

of O^{2-} in the nanoferrites [38, 39]. The narrow scan spectrum of Co 2p as noticed from Fig. 6c, and corresponding two peaks at 778.93 and 786 ± 0.4 eV. Similarly 785.11 eV and 790 ± 15 were present for Co $2p^{3/2}$ and Co $2p^{1/2}$, which confirms the oxidation state of Co^{2+} . The narrow range spectrum of Fe 2p in nanoferrites revealed Fe $2p^{3/2}$ and Fe $2p^{1/2}$ binding energy peaks at 709.75 and 718 ± 0.8 eV for Fe $2p^{3/2}$, 723.54 and 725 ± 14 eV for Fe $2p^{1/2}$ Fig. 6a, respectively. The peak at 718 ± 0.8 eV is attained due to the Fe^{3+} cation located at the octahedral site in the spinal ferrites, and the peak at 725 ± 14 eV is attained due to the Fe^{2+} cation located at the tetrahedral site in the spinal ferrites [39, 40]. From Fig. 6d, the narrow scan spectrum was obtained for La^{3+} with binding energies of 833.18 ± 0.69 eV for $3d^{5/2}$

and 837.20 ± 0.12 eV for $3d^{3/2}$. The obtained peaks were explained to the electron transfer of oxygen to the 4 f sub-shell of La^{3+} ions due to photo-ionization process [38]. From XRD and XPS results, it was clearly noticed that the La^{3+} ions were assimilated into Fe ions in cobalt nanoferrites. The observed binding energy of oxygen, cobalt, iron, and lanthanum is listed in Table 4.

3.6 Magnetic properties

The M-H loop for prepared $\text{CoLa}_x\text{Fe}_{2-x}\text{O}_4$ nanoferrites have been plotted with magnetic field maximum of $15,000$ Oe at room temperature by VSM. From Fig. 7, S shaped hysteresis loops shows the soft magnetic nature of the prepared

Table 4 Binding energy of prepared $\text{CoLa}_x\text{Fe}_{2-x}\text{O}_4$ ($X=0.00$ to 0.08) nanoferrites

Composition	O 1s (eV)	Co 2p (eV)		Fe 2p (eV)		La 3d (eV)	
		$2p^{3/2}$	$2p^{1/2}$	$2p^{3/2}$	$2p^{1/2}$	$3d^{5/2}$	$3d^{3/2}$
$X=0.00$	529.06	778.93	785.11	709.75	723.58	-	-
$X=0.02$	535.76	786.98	790.28	718.49	725.16	833.18	837.20
$X=0.08$	535.96	787.12	790.43	718.57	725.30	833.87	837.32

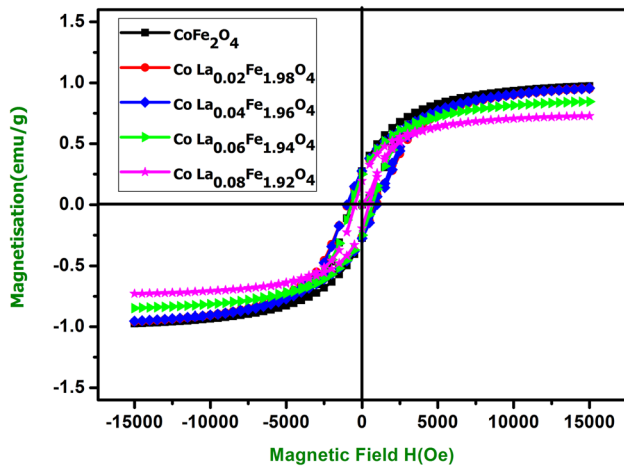


Fig. 7 Hysteresis loop of the prepared $\text{CoLa}_x\text{Fe}_{2-x}\text{O}_4$ ($X=0.00$ to 0.08) nanoferrites

nanoferrites. The variation in magnetic parameters such as coercivity (H_c), magnetic saturation (M_s), retentivity (M_r), and magnetic moment (η_B) for prepared nanoferrites have been revealed to be dependent of number of factors such as grain growth, anisotropy, density, A–B exchange interaction, surface spin effect, synthesis techniques, and chemical composition [41].

From magnetic hysteresis loops, it is understood that the inclusion of La^{3+} ions promotes ferromagnetic nature. From Table 5, it is noticed the values of saturation magnetization decreases with an increase in La^{3+} ions in CoFe_2O_4 nanoparticles which could be explained by Neel's sublattice model [42]. From the Neel's sub lattice model, the magnetic moment of ions on the A-site and B-site sublattices was aligned antiparallel to each other and their spins have a collinear structure. The magnetic moment was calculated by using the following equation:

$$\eta_B = M_B - M_A \quad (9)$$

where M_A and M_B are [A] and [B] sublattices [43]. In general, magnetic super exchange interaction is based on the cation distribution between A-site and B-sites. This could

be attained due to their larger ionic radii. Therefore, suggesting that the nonmagnetic La^{3+} could be replacing Fe^{3+} ions from octahedral site (B) to tetrahedral site (A) [44]. Moreover, three types of exchange interaction would have happened between the magnetic ion at octahedral (B) and tetrahedral (A) sites in spinel structure such as AA interaction, BB interaction, AB interaction.

Out of three mentioned interactions, AB interaction predominates over rest of other two interactions [41]. Further, the increase in La^{3+} ions in $\text{CoLa}_x\text{Fe}_{2-x}\text{O}_4$ nanoparticles decreases the value of M_s from 97.35 to 75.84 emu/g with a decrease in crystal size from 42 to 18 nm, which results in the increase in the surface effect [43, 44]. Decreasing crystallite size due to the substitution of La^{3+} trends to the increase in disordered spins which implies in the decrease in magnetic saturation. The value of coercivity increases from 736.33 to 1128.35 Oe with an increase in La^{3+} ions depending on crystal size, magnetic crystallite, cation distribution, strain, porosity, and anisotropy [45]. According to Brown's relation, the coercivity is inversely proportional to the magnetic saturation. It was agreed for the prepared nanoferrites, where the coercivity increased with decreasing magnetic saturation for addition of La^{3+} concentration. The anisotropy constant and squareness ratio were estimated by using the following equation [46, 47]:

$$\frac{M_r}{M_s} \quad (10)$$

$$K = \frac{H_c M_s}{0.98} \quad (11)$$

where M_r is the remanent magnetization or retentivity, K is the anisotropy constant. Further, Bohr magnetizations (η_B) in magnetic moments (μ_B) were estimated from the following equation [47]:

$$\eta_B = \frac{MXM_s}{5585} \quad (12)$$

where X is the concentration and M is the molecular weight of La^{3+} ion content. The magnetic parameters such as magnetic saturation (M_s), coercivity (H_c), retentivity (M_r),

Table 5 Magnetic parameters of prepared $\text{CoLa}_x\text{Fe}_{2-x}\text{O}_4$ ($X=0.00$ to 0.08) nanoferrites

Composition	Magnetization (M_s) (emu/g)	Remanent magnetization (M_r) (emu/g)	Coercivity (H_c) (Oe)	Squareness ratio (M_r/M_s) (No unit)	Anisotropy constant (K) (Oe)	Bohr magneton (η_B) (μ_B)
$X=0.00$	97.35	27.45	736.33	0.2819	73.14	0.4381
$X=0.02$	95.62	26.75	958.91	0.2797	93.56	0.4273
$X=0.04$	95.59	25.64	993.84	0.2683	96.90	0.4241
$X=0.06$	94.66	25.04	1010.45	0.2645	63.60	0.3731
$X=0.08$	75.84	19.45	1128.23	0.2564	34.94	0.3188

squareness ratio, anisotropic constant (k) and Bohr magneton (n_B) were noticed from M–H and measurements are listed in Table 5. This suggests that $\text{CoLa}_x\text{Fe}_{2-x}\text{O}_4$ nanoferrites have spin arrangements which are better on the B-site, leading to decrease in (A–B interaction) [48, 49]. It was observed that the addition of La^{3+} ions in cobalt matrix improved to get soft ferrite behavior with good saturation magnetization and it has good suitability for electromagnetic application [50]

3.7 Impedance analysis

Impedance spectroscopy is a well-known technique for complete understanding of electrical properties of spinel type ferrites, whose properties depend on their ceramic texture, impedance of electrodes, distribution of dopants and grain and grain boundary contributions [51]. And it also provides information regarding imaginary and real components of the impedance property of a material. The Nyquist plot shows a complete contribution of grain and grain boundary resistance. Figure 8c shows that the applied frequency dependent imaginary (Z'') and real (Z') part of impedance decreased with an increase in frequency. It denotes an increase in a.c conductivity. The real part (Z') of the spectra values for all the prepared nanoparticles leads to lower values at higher frequency which implies release of space charges as a result of reduction in barrier properties of material [51]. In Fig. 8a, impedance vs frequency plot gives an indication of a increase in conduction with frequency, which infers that the ferrites behave like a semiconductor material [52].

Figure 8b, the imaginary part (Z'') of the La^{3+} -doped cobalt nanoferrites decreases with an increase in applied frequency and then remains low at high frequency. The imaginary part (Z'') of the impedance spectra brings out relaxation peaks due to existence of space charge relaxation, associated with charge carries resulting from energy vacancies [53]. The Z'' also decreases with increasing frequency due to the decreasing loss in the imaginary part of the nanoferrites.

Nyquist plot of impedance spectra as function of frequency for $\text{CoLa}_x\text{Fe}_{2-x}\text{O}_4$ nanoferrites is shown in Fig. 8c. Clear semicircle arcs were formed in high frequency for all the prepared nanoferrites with series of ($X=0.00$ to 0.08) because of the grain and grain boundary contributions to the conductivity. This also indicates that because of small crystal size, the grain boundary contribution is higher than that of the grain contribution [54]. Furthermore, it is observed that the value of Z' and Z'' in the impedance spectra for cobalt decreases with increasing La^{3+} concentration and it depicts that the overall resistance of the La^{3+} -doped cobalt ferrite nanoparticles decreases, accordingly.

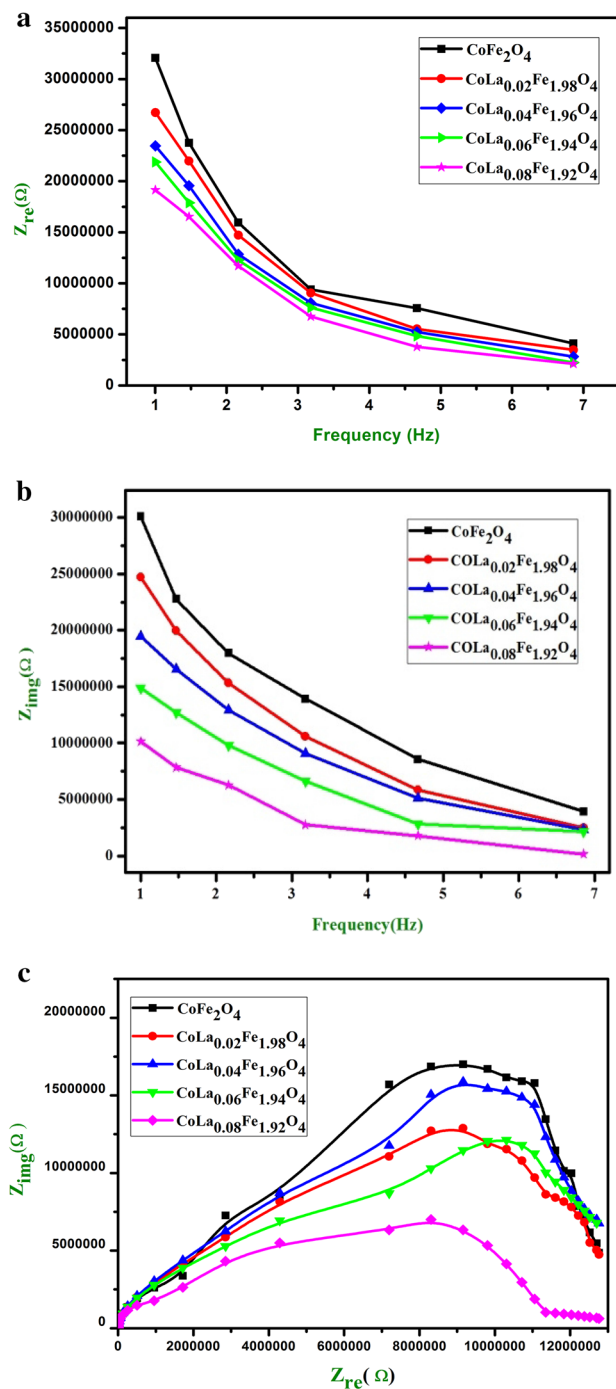


Fig. 8 **a** Real part of impedance spectra of prepared $\text{CoLa}_x\text{Fe}_{2-x}\text{O}_4$ ($X=0.00$ to 0.08) nanoferrites. **b** Imaginary part of impedance spectra of prepared $\text{CoLa}_x\text{Fe}_{2-x}\text{O}_4$ ($X=0.00$ to 0.08) nanoferrites. **c** Nyquist plots of prepared $\text{CoLa}_x\text{Fe}_{2-x}\text{O}_4$ ($X=0.00$ to 0.08) nanoferrites

3.8 Dielectric properties

3.8.1 Dielectric constant

The variation of dielectric constant (ϵ') measured at the frequency in microhertz at RT for the prepared nanoferrites as shown in Fig. 9a. The dielectric constant decreases with an increase in lanthanum content as a mechanism for the electrical conduction, which is same that of dielectric polarization. The dielectric constant was calculated using the following equation [44]:

$$\epsilon' = \frac{Cd}{\epsilon_0 A} \quad (13)$$

where ϵ' is the dielectric constant, C is the capacitance of the pellet, ϵ_0 is the permittivity of free space, A is the area of the $\text{CoLa}_X\text{Fe}_{2-X}\text{O}_4$ pellet, and d is the thickness of the pellet. The values of dielectric constant both ϵ' and ϵ'' are higher

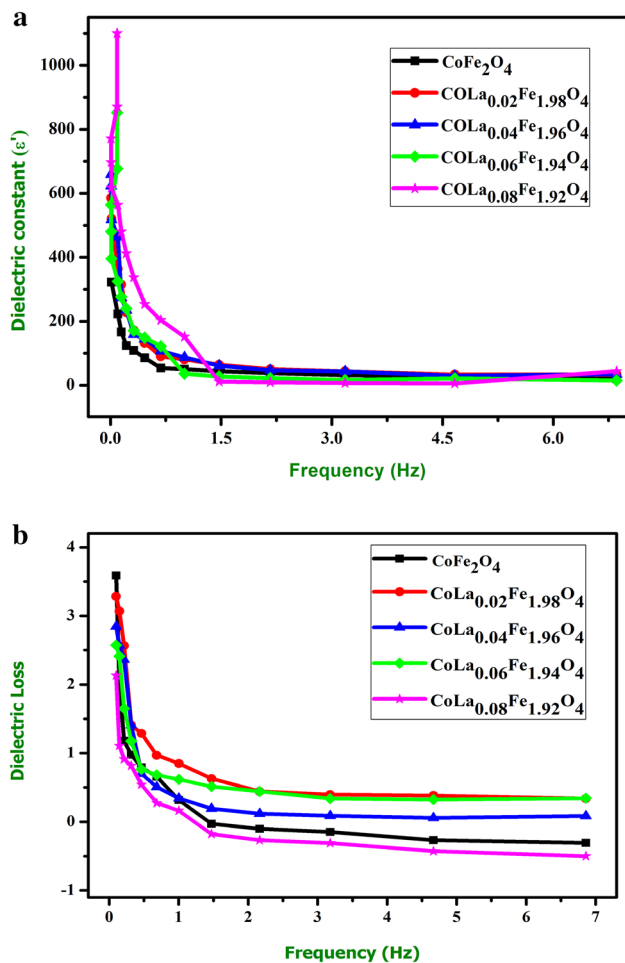


Fig. 9 **a** Dielectric constant of the prepared $\text{CoLa}_X\text{Fe}_{2-X}\text{O}_4$ ($X=0.00$ to 0.08) nanoferrites, **b** Dielectric loss of the prepared $\text{CoLa}_X\text{Fe}_{2-X}\text{O}_4$ ($X=0.00$ to 0.08) nanoferrites

at lower frequency and then decreases with an increase in frequency for all the compositions ($X=0.00$ to 0.08).

The obtained dielectric constant and complex dielectric constant values are 321, 585, 659, 852, and 1100 and 1150, 1921, 1874, 2190, and 2344 for all the compositions of $X=0.00, 0.02, 0.04, 0.06,$ and 0.08 , respectively. The dielectric constants at lower frequency are based on some polarizations such as ionic, space charges, and interface [55, 56]. This type of behavior can be described based on Maxwell–Wagner interfacial polarization which is in agreement with Koop’s theory [57]. According to the Maxwell–Wagner model, the dielectric constant was due to high conductivity grains and poor conductivity grain boundaries.

In $\text{CoLa}_X\text{Fe}_{2-X}\text{O}_4$ spinel ferrites, the formation of Fe^{2+} ions are due to interchange of electrons between Co^{2+} and Fe^{3+} to generate a pair of Co^{3+} and Fe^{2+} ions [58]. The electron hopping between $\text{Fe}^{2+} \leftrightarrow \text{Fe}^{3+}$ and hole hopping between $\text{Co}^{3+} \leftrightarrow \text{Co}^{2+}$ ions and hence an applied electric field, the electrons pile up there, due to high resistance ultimately produces polarization. However, at high frequency the electron cannot move with fast changes due to the applied electric field because charge carries need sufficient time to transfer their orientation in react to the applied electric field. In general, the dielectric constant of any surface material depends on bulk polarization factor such dipolar, interfacial, ionic, and electronic polarizations. In certain polarizations, dipolar and interfacial polarizations are real for the noticed behavior in dielectric constant at lower frequency, while electronic polarization is held responsible in the high-frequency region [59]. The decrease in both ϵ'' and ϵ' with frequency is due to the fact that any species contributing to polarization is bound to slow the logging behind the applied field at high frequency [60, 61]. Interestingly dielectric constant values decreased by more than 50% from 1100 ($X=0.08$) to 321 ($X=0.00$) when the La^{3+} increased less than 0.1% in $\text{CoLa}_X\text{Fe}_{2-X}\text{O}_4$. The substitution of La^{3+} ions in $\text{CoLa}_X\text{Fe}_{2-X}\text{O}_4$ nanoferrites tends to have significant variation in ϵ' which improves the suitability of the nanoferrites for microwave frequency applications.

3.8.2 Dielectric loss

The variation of dielectric loss or loss tangent with variation of frequency is shown in Fig. 9b. It is evidently noticed that the loss tangent decreases with an increase in La^{3+} concentration. This can be mainly due to the increase in resistivity which results loss in $\tan\delta$. From the results, it is observed that the dielectric loss decreases with an increase in frequency at low frequency which decreased slowly in high-frequency region before it become almost independence of the frequency in the higher-frequency region.

The dielectric loss is formulated with high resistivity at low frequency which is playing major role. The dielectric

Table 6 Dielectric parameters of prepared $\text{CoLa}_x\text{Fe}_{2-x}\text{O}_4$ ($X=0.00$ to 0.08) nanoferrites

Composition	Dielectric constant (ϵ')	Dielectric loss ($\tan\delta$)	Complex dielectric constant (ϵ'')
$X=0.00$	321	3.583	1150.14
$X=0.02$	585	3.284	1921.44
$X=0.04$	659	2.844	1874.19
$X=0.06$	852	2.571	2190.49
$X=0.08$	1100	2.131	2344.10

loss and complex dielectric constant of nanoferrites were calculated using following equations [62]:

$$\tan \delta = \frac{1}{2\pi f \epsilon_0 \epsilon'} \quad (14)$$

$$\epsilon'' = \epsilon' \tan \delta \quad (15)$$

The dielectric losses of the nanoferrites are 3.583, 3.284, 2.844, 2.571, and 2.131, respectively. The electron interchange between Fe^{2+} and Fe^{3+} required more energy and accordingly more energy ions due to high resistivity of grain boundaries [63]. Further, the electron interchange between Fe^{2+} and Fe^{3+} required loss of energy at high frequency of applied AC electric field which is equal to the hopping frequency of the charge carrier. The large amount of energy was thus recovered to transfer the oscillating ions and those by appearance of dielectric loss. The prepared material shows low dielectric loss is favorable for application in micro frequency devices. The electrical parameters such as dielectric constant, dielectric loss, and complex dielectrics are listed in Table 6.

4 Conclusion

Lanthanum-doped cobalt $\text{CoLa}_x\text{Fe}_{2-x}\text{O}_4$ nanoferrites with various composition for $X=0.00, 0.02, 0.04, 0.06, 0.08$ were synthesized using simple and most effective sol–gel technique. XRD revealed cubic spinel structure with an average crystal size of 31 nm. FTIR analyses confirmed the presence of metal at 583 cm^{-1} corresponding to stretching M–O bond, respectively. The lattice constant and volume of unit cell were increased with an increase in La^{3+} ions, whereas X-ray density and bulk density became inversely proportional to lattice constant. UV diffuse reflectance spectra showed that the absorbance spectra of the $\text{CoLa}_x\text{Fe}_{2-x}\text{O}_4$ nanoferrite were varied from 226 to 222 nm. The value of indirect and direct energy bandgap varied from 1.73 to 2.06 eV and 1.45 to 1.56 eV. The obtained bandgap energy increased with an increase in La^{3+} concentrations. The obtained prepared

nanoferrites were identified with spherical morphology. XPS confirmed the presence of Co 2p, Fe 2p, La 3d, and O 1s at octahedral [B] and tetrahedral [A] sites in $\text{CoLa}_x\text{Fe}_{2-x}\text{O}_4$ nanoferrites. The obtained VSM result showed that the prepared lanthanum-doped cobalt nanoferrites has got a soft ferromagnetic nature. The saturation magnetization from 97.35 to 75.84 emu/g decreases with an increase in La^{3+} concentration. The higher coercivity (1128 Oe) with dielectric constant of the lanthanum-doped cobalt spinel nanoferrites is favorable for the applications in magneto recording devices. Impedance spectroscopy is used to identify grain contributions and grain boundary contributions to conductivity and utilized to estimate electrical response of lanthanum-doped cobalt nanoferrites. The frequency-dependant dielectric constant, complex dielectric constant, and dielectric loss decreases with an increase in La^{3+} ion. Behavior of dielectric constant and AC conductivity of pure and lanthanum-doped cobalt nanoferrites was found to follow Maxwell–Wagner’s model. Hence the combination of structural, magnetic, electrical, and optical activities makes $\text{CoLa}_x\text{Fe}_{2-x}\text{O}_4$ ($X=0.00$ to 0.08) nanoferrites highly useful for reducing false signals in the electronic devices and its highly suitable for microwave frequency applications.

References

- R.S. Yadava, I. Kuritkaa, J. Vilcakovaa, J. Havlicab, L. Kalinab, P. Urbaneka, M. Machovskya, D. Skodaa, M. Masara, M. Holeka, Sonochemical synthesis of Gd^{3+} doped CoFe_2O_4 spinel ferrite nanoparticles and its physical properties. *Ultrason. Sonochem.* **40**, 773–783 (2018)
- A. Kovalenko, R.S. Yadav, J. Pospisil, O. Zmeskal, D. Karashanova, P. Heinrichova, M. Vala, J. Havlica, M. Weiter, Towards improved efficiency of bulk-heterojunction. Solar cells using various spinel ferrite magnetic nanoparticles. *Org. Electron.* **39**, 118–126 (2016)
- P.N. Anantharamaiah, P.A. Joy, Tuning of the magnetostrictive properties of cobalt ferrite by forced distribution of substituted divalent metal ions at different crystallographic sites. *J. Appl. Phys.* **121**, 093904 (2017)
- X. Lasheras, M. Insausti, I. Gil de Muro, E. Garaio, F. Plazaola, M. Moros, L. De, J.M. de la Matteis, L.L. Fuente, Chemical synthesis and magnetic properties of monodisperse nickel ferrite nanoparticles for biomedical applications. *J. Phys. Chem. C* **120**(6), 3492–3500 (2016)
- L. Kumar, M. Kar, Effect of La^{3+} substitution on the structural and magneto crystalline anisotropy of nanocrystalline cobalt ferrite ($\text{CoFe}_{2-x}\text{La}_x\text{O}_4$). *Ceram. Int.* **438**, 4771–4778 (2012)
- K. Pubby, S.S. Meena, S.M. Yusuf, S.B. Narang, Cobalt substituted nickel ferrites via Pechini’s sol-gel route: X-band electromagnetic characterization. *J. Magn. Magn. Mater.* **466**, 430–445 (2018)
- L.T. Lu, N.T. Dung, L.D. Tung, C.T. Thanh, O.K. Quy, N.V. Chuc, S. Maenosono, N.T.K. Thanh, Synthesis of magnetic cobalt ferrite nanoparticles with controlled morphology, mono dispersity and composition: the influence of solvent, surfactant, reductant and synthetic conditions. *Nanoscale* **7**, 19596 (2015)

8. H. Widatallah, C. Johnson, A. Gismelseed, I. Al-Omari, S. Stewart, S. Al-Harathi, S. Thomas, H. Sitepu, Structural and magnetic studies of nanocrystalline Mg-doped $\text{Li}_0.5\text{Fe}_2.5\text{O}_4$ particles prepared by mechanical milling. *J. Phys. D* **41**, 165006 (2008)
9. S.K. Gore, S.S. Jadhav, V.V. Jadhav, S.M. Patange, M. Naushad, R.S. Mane, K.H. Kim, The structural and magnetic properties of dual phase cobalt ferrite. *Sci. Rep.* **7**, 2524 (2017)
10. K.K. Bharathi, R.J. Tackett, C.E. Botez, C.V. Ramana, Coexistence of spin glass behavior and long-range ferromagnetic ordering in La- and Dy-doped Co ferrite. *J. Appl. Phys.* **109**, 07A510 (2011)
11. N. Lenin, R.R. Kanna, K. Sakthipandi, A.S. Kumar, Structural, electrical and magnetic properties of $\text{NiLa}_x\text{Fe}_{2-x}\text{O}_4$ nanoferrites. *Mater. Chem Phys.* **212**, 385–393 (2018)
12. J. Azadmanjiri, H.K. Salehani, M.R. Barati, F. Farzan, Preparation and electromagnetic properties of $\text{Ni}_{1-x}\text{Cu}_x\text{Fe}_2\text{O}_4$ nanoparticle ferrites by sol-gel auto combustion method. *Mater. Lett.* **61**, 84–87 (2007)
13. H. Wang, H. Guo, Y. Dai, D. Geng, Z. Han, D. Li, T. Yang, S. Ma, W. Liu, Z. Zhang, Optimal electromagnetic-wave absorption by enhanced dipole polarization in Ni/C nanocapsules. *Appl. Phys. Lett.* **101**, 083116 (2012)
14. V. Chaudhari, S.E. Shirsath, M.L. Mane, R.H. Kadam, S.B. Shelke, D.R. Mane, Crystallographic, magnetic and electrical properties of $\text{Ni}_{0.5}\text{Cu}_{0.25}\text{Zn}_{0.25}\text{La}_x\text{Fe}_{2-x}\text{O}_4$ nanoparticles fabricated by solgel method. *J. Alloys Compd.* **549**, 213–220 (2013)
15. P.K. Roy, J. Bera, Enhancement of the magnetic properties of Ni-Cu-Zn ferrites with the substitution of a small fraction of lanthanum for iron. *Mater. Res. Bull.* **42**, 77–83 (2007)
16. M.R. Kadam, R.P. Patil, P.P. Hankare, Investigations on structural, electrical and magnetic properties of nickel substituted La-ferrites. *Solid State Sci.* **14**, 964–970 (2012)
17. R.R. Kanna, N. Lenin, K. Sakthipandi, M. Sivabharathy, Impact of Lanthanum on structural, optical, dielectric and magnetic properties of $\text{Mn}_{1-x}\text{Cu}_x\text{Fe}_{1.85}\text{La}_{0.15}\text{O}_4$ spinel nanoferrites. *Ceram. Int.* **43**, 15868–15879 (2017)
18. K. Sakthipandi, V. Rajendran, T. Jayakumar, B. Raj, P. Kulandivelu, Synthesis and on-line ultrasonic characterisation of bulk and nanocrystalline $\text{La}_{0.68}\text{Sr}_{0.32}\text{MnO}_3$ perovskite manganite. *J. Alloys Compd.* **509**, 3457–3467 (2011)
19. A.M. Anwar, Enhancement of electrical and magnetic properties of Cd^{2+} doped Mn-Zn soft nanoferrites prepared by the sol-gel autocombustion method. *J. Magn. Magn. Mater.* **333**, 46–52 (2013)
20. Z. Yan, J. Gao, Y. Li, M. Zhang, M. Guo, Hydrothermal synthesis and structure evolution of metal-doped magnesium ferrite from saprolite laterite. *RSC Adv.* **5**, 92778–92787 (2015)
21. J. de Vicente, A.V. Delgado, R.C. Plaza, J.D.G. Duran, F.G. Caballero, Stability of Cobalt ferrite colloidal particles. Effect of pH and applied magnetic fields. *Langmuir* **16**, 7954–7961 (2000)
22. F. Bensebaa, L. Zavaliche, P. Ecuier, R.W. Cochrane, T. Veres, Microwave synthesis and characterization of co-ferrite nanoparticles. *J. Colloid Interface Sci.* **277**, 104–110 (2004)
23. S. Gaba, A. Kumar, P.S. Rana, M. Arora, Influence of La^{3+} ion doping on physical properties of magnesium nanoferrites for microwave absorption application. *J. Magn. Magn. Mater.* **S0304-8853**, 32557 (2017)
24. B. Vigneshwaran, P. Kuppusami, A. Panda, A. Singh, H. Sreemoolanadhan, Microstructure and optical properties of $\text{Ba}_{0.6}\text{Sr}_{0.4}\text{TiO}_3$ thin films prepared by pulsed laser deposition. *Mater. Res. Express* **5**, 0664 (2018)
25. A. Sattar, A.M. Samy, R.S. El-Ezza, A.E. Eatah, Effect of rare-earth substitution on magnetic and electrical properties of Mn-Zn ferrites. *Phys. Status Solid* **193**(1), 86–93 (2002)
26. M.I. Ali, U. Islam, M.I. Hasan, M. Khan, M.N. Ashiq, Effect of Gd-substitution on physical and magnetic properties of $\text{Li}_{1.2}\text{Mg}_{0.4}\text{Gd}_x\text{Fe}_{(2-x)}\text{O}_4$ ferrites. *J. Alloys Compd.* **579**, 181–186 (2013)
27. R.S. Yadav, J. Havlica, J. Masilko, L. Kalina, J. Wasserbauer, M. Hajduchova, V. Enev, I. Kuritka, Z. Kozakova, Impact of Nd^{3+} in CoFe_2O_4 spinel ferrite nanoparticles on cation distribution, structural and magnetic properties. *J. Magn. Magn. Mater.* **399**, 109–117 (2015)
28. J. Peng, M. Hojamberdiev, Y. Xu, B. Cao, J. Wang, H. Wu, Structural and Electrical Studies of $\text{MnGd}_x\text{Fe}_{2-x}\text{O}_4$ Nanoparticles. *J. Magn. Magn. Mater.* **323**, 133–138 (2011)
29. I. Ali, M. Ahmad, M.U. Islam, M.S. Awan, *Substitution effects of La^{3+} ions on the structural and magnetic properties of Co_2Y hexaferrites synthesized by sol-gel autocombustion method* (Springer, New York, 2013)
30. E.R. Kumar, T. Prakash, Heat treatment effects on structural and dielectric properties of Mn substituted CuFe_2O_4 and ZnFe_2O_4 nanoparticles. *J. Superlatt. Microstruct.* **85**, 530–535 (2015)
31. L. Saravanan, R. Jayavel, A. Pandurangan, J.H. Liu, H.Y. Miao, Synthesis, structural and optical properties of Sm^{3+} and Nd^{3+} doped cadmium sulfide nanocrystals. *Mater. Res. Bull.* **52**, 128 (2014)
32. P.P. Hankare, R.P. Patil, A.V. Jadhav, R.S. Pandav, K.M. Garadkar, R. Sasikala, A.K. Tripathi, Synthesis and characterization of nanocrystalline Ti-substituted Zn ferrite. *J. Alloy. Compd.* **509**, 2160–2163 (2011)
33. G. Mustafa, M.U. Islam, M. Ahmad, W. Zhang, Y. Jamil, A. Wahee, A.M. Hussain, Influence of the divalent and trivalent ions substitution on the structural and magnetic properties of $\text{Mg}_{0.5-x}\text{Cd}_x\text{Co}_{0.5}\text{Cr}_{0.04}\text{Tb}_{1.96-y}\text{O}_4$ ferrites prepared by sol-gel method. *J. Magn. Magn. Mater.* **387**, 147–154 (2015)
34. P.P. Hankare, K.R. Sanadi, K.M. Garadkar, D.R. Patil, I.S. Mulla, Synthesis and characterization of nickel substituted cobalt ferrite nanoparticles by sol-gel auto-combustion method. *J. Alloys Compd.* **553**, 383–388 (2013)
35. J. Peng, M. Hojamberdiev, Y. Xu, B. Cao, J. Wang, H. Wu, Hydrothermal synthesis and magnetic properties of gadolinium-doped CoFe_2O_4 nanoparticles. *J. Magn. Magn. Mater.* **323**, 133–138 (2011)
36. P.S. Aghav, V.N. Dhage, M.L. Mane, D.R. Shengule, R.G. Dorik, K.M. Jadhav, Effect of aluminium substitution on the structural and magnetic properties of cobalt ferrite synthesized by sol-gel auto combustion process. *Phys. B* **406**, 4350–4354 (2011)
37. M.H. Abdellatif, C. Innocenti, I. Liakos, A. Scarpellini, S. Marras, M. Salerno, Effect of Jahn-Teller distortion on the short range magnetic order in copper ferrite. *J. Magn. Magn. Mater.* **424**, 402–409 (2017)
38. S. Anandan, T. Selvamani, G.G. Prasad, A.M. Asiri, J.J. Wu, Magnetic and catalytic properties of inversespinel CuFe_2O_4 nanoparticles. *J. Magn. Magn. Mater.* **43**, 437–443 (2017)
39. N. Venkatesha, S.M. Pudukalakatti, Y. Qurishi, H.S. Atreya, C. Srivastava, MnFe_2O_4 - Fe_3O_4 core-shell nanoparticles as potential contrast agent for magnetic resonance imaging. *RSC Adv.* **5**, 97807–97815 (2015)
40. Z.K. Karakas, R. Boncukcuoglu, I.H. Karakas, The effects of heat treatment on the synthesis of nickel ferrite (NiFe_2O_4) nanoparticles using the microwave assisted combustion method. *J. Magn. Magn. Mater.* **374**, 298–306 (2015)
41. R.S. Yadav, I. Kuritka, J. Vilcakova, J. Havlica, J. Masilko, L. Kalina, J. Tkacz, J. Svec, V. Enev, M. Hajduchov, Impact of grain size and structural changes on magnetic, dielectric, electrical, impedance and modulus spectroscopic characteristics of CoFe_2O_4 nanoparticles synthesized by honey mediated sol-gel combustion method. *Adv. Nat. Sci.* **8**, 045002 (2017)
42. H.S. Aziz, S. Rasheed, R.A. Khan, A. Rahim, J. Nisar, S.M. Shah, F. Iqbal, A.R. Khan, Evaluation of electrical, dielectric and

- magnetic characteristics of Al-La doped nickel spinel ferrites. *RSC Adv.* **6**, 6589–6597 (2016)
43. Y.K. Dasan, B.H. Guan, M.H.Z. Chuan, Influence of La³⁺ substitution on structure, morphology and magnetic properties of nanocrystalline Ni-Zn ferrite. *PLoS ONE* **12**(1), e0170075 (2017)
 44. B. Santosh, N. Tsering, S. Mor, S. Bansal, S. Singhal, Structural, electrical, optical and magnetic properties of chromium substituted Co-Zn nanoferrites Co_{0.6}Zn_{0.4}Cr_xFe_{2-x}O₄ (0 ≤ x ≤ 1.0) prepared via sol-gel auto-combustion method. *J. Mol. Struct.* **1012**, 162–167 (2012)
 45. S. Joshi, M. Kumar, S. Chhoker, A. Kumar, M. Singh, Effect of Gd³⁺ substitution on structural, magnetic, dielectric and optical-properties of nanocrystalline CoFe₂O₄. *J. Magn. Magn. Mater.* **426**, 252–263 (2017)
 46. H. Anwar, A. Maqsood, Structural, magnetic and electrical properties of Cu substituted Mn Zn soft nanoferrites. *J. Supercond. Nov. Magn.* **25**, 1913–1920 (2012)
 47. Y. Zhou, W. Chen, Y. Shen, X. Wu, W. Wu, J. Wu, Lattice strains and magnetic properties evolution of copper-magnesium ferrite with lithium substitution. *J. Magn. Magn. Mater.* **396**, 198–203 (2015)
 48. R. Tholkappiyan, K. Vishista, Influence of lanthanum on the optomagnetic properties of zinc ferrite prepared by combustion method. *Phys. B* **448**, 177–183 (2014)
 49. K.K. Kefeni, T.A.M. Msagati, B.B. Mamba, Ferrite nanoparticles: synthesis, characterisation and applications in electronic device. *Mater. Sci. Eng. B* **215**, 37–55 (2017)
 50. K. Lily, K. Kumari, R.N. Prasad, P. Choudhary, Impedance spectroscopy of (Na_{0.5}Bi_{0.5})(Zr_{0.25}Ti_{0.75})O₃ lead-free ceramic. *J. Alloy. Compd.* **453**, 325–331 (2008)
 51. M.A. Rahman, A.K.M.A. Hossain, Electrical transport properties of Mn-Ni-Zn ferrite using complex impedance spectroscopy. *Phys. Scr.* **89**, 025803 (2014)
 52. R.V. Mangalaraja, S. Ananthakumar, P. Manohar, F.D. Gnanam, Magnetic, electrical and dielectric behaviour of Ni_{0.8}Zn_{0.2}Fe₂O₄ prepared through flash combustion technique. *J. Magn. Magn. Mater.* **253**, 56–64 (2002)
 53. C. Murugesan, G. Chandrasekaran, Impact of Gd³⁺ substitution on the structural, magnetic and electrical properties of cobalt ferrite nanoparticles. *RSC Adv.* **5**, 73714–73725 (2015)
 54. D.M. Jnaneshwara, D.N. Avadhani, B. Daruka Prasad, H. Nagabhushana, B.M. Nagabhushana, S.C. Sharma, S.C. Prashantha, C. Shivakumar, Role of Cu²⁺ ions substitution in magnetic and conductivity behaviour of nano CoFe₂O₄. *Spectrochim. Acta Part A* **132**, 256–262 (2014)
 55. J. Parashar, V.K. Saxena, D. Jyoti, K.B. Bhatnagar, Sharma, Dielectric behaviour of Zn substituted Cu nano-ferrites. *J. Magn. Magn. Mater.* **394**, 105–110 (2015)
 56. D. Ravinder, P.V.B. Reddy, High-frequency dielectric behaviour of Li-Mg ferrites. *Mater. Lett.* **57**, 4344–4350 (2003)
 57. G.R. Mohan, D. Ravinder, A.V.R. Reddy, B.S. Boyanov, Dielectric properties of polycrystalline mixed nickel-zinc ferrites. *Mater. Lett.* **40**, 39–45 (1999)
 58. M.J. Iqbal, R.A. Khan, S. Mizukami, T. Miyazaki, Mossbauer, magnetic and microwave absorption characteristics of substituted W-type hexaferrites nanoparticles. *Ceram. Int.* **38**, 4097–4103 (2012)
 59. R.K. Kotnala, Preparation and characterization chemistry of nanocrystalline NiCuZn ferrite. *J. Alloys Compd.* **549**, 348–357 (2013)
 60. M.H. Alimuddin, S.E. Shirsath, S. Kumar, R. Kumar, A.S. Roy, J. Shah, R.K. Kotnala, Preparation and characterization chemistry of nano-crystalline NiCuZn ferrite. *J. Alloys Compd.* **549**, 348–357 (2013)
 61. S.F. Mansour, Frequency and composition dependence on the dielectric properties for Mg-Zn ferrite. *Egypt. J. Solids* **28**(2), 211–214 (2005)
 62. Z.C. Veji, S. Raki, S. Jankov, S. Skuban, A. Kapor, Dielectric properties and conductivity of zinc ferrite and zinc ferrite doped with yttrium. *J. Alloy. Compd.* **480**, 241–245 (2009)
 63. S.A. Saafan, S.T. Assar, Dielectric behavior of nano-structured and bulk LiNiZn ferrite samples. *J. Magn. Magn. Mater.* **324**, 2989–3001 (2012)
- Publisher's Note** Springer Nature remains neutral with regard to jurisdictional claims in published maps and institutional affiliations.